ELSEVIER

Contents lists available at ScienceDirect

Journal of Materials Research and Technology

journal homepage: www.elsevier.com/locate/jmrt





Incorporating bulk microstructural and surface properties to predict the performance of high chromium cast irons – indentation behaviour and wear performance

U. Pranav Nayak ^{a,*} ^o, Bruno Alderete ^a ^o, Sebastian Suarez ^a ^o, María Agustina Guitar ^a ^o, Frank Mücklich ^{a,b}

ARTICLE INFO

Handling Editor: Prof. M Meyers

Keywords:
Hypoeutectic high chromium cast iron
Spherical indentation
Plastic deformation
Wear performance
Microstructure characterization

ABSTRACT

This study investigates the indentation behaviour and wear performance of two hypoeutectic high chromium cast iron alloys with 16 % and 26 % chromium. Indentations were performed using an alumina spherical ball at various loads, and the resulting contact radii (ranging from ~30 μm to 50 μm) were compared with Hertzian predictions. A novel methodology using image segmentation was developed to estimate bulk mechanical properties using local phase distribution. Plasticity index calculations, incorporating both matrix and carbide surface characteristics, yielded comparable values (~29) for both alloys, indicating similar elastic-plastic contact responses despite differences in carbide size and volume fraction. Abbott-Firestone curve analysis revealed that 26 % Cr alloy exhibited slightly higher bearing capacity at shallow depths. Subsequent wear tests showed that under low load conditions (5 N), the 26 % Cr alloy exhibited lower wear rates compared to the 16 % Cr alloy. However, at 20 N, the difference falls within the standard deviation, suggesting that both alloys perform similarly under high-load wear.

1. Introduction

High chromium cast irons (HCCIs) are a category of abrasion-resistant white cast irons known for their exceptional combination of abrasion resistance and toughness [1,2]. These materials contain between 11 and 30 wt% chromium (Cr) and 2–4 wt% carbon (C), forming part of the Fe–Cr–C ternary system as outlined in the ASTM A532 standard [3,4]. The microstructures of HCCIs are characterized by hard M_7C_3 (M: Cr, Fe) eutectic carbides (EC) dispersed within a supportive and modifiable matrix that can be austenite, ferrite, or martensite [5–7]. This composition results in HCCI microstructures possessing up to 50 % carbides by volume, with hardness values ranging between 1200 and 1600 HV [8,9]. The carbides provide the hardness and wear resistance, whereas the matrix contributes to the material's toughness [10].

HCCIs are extensively used in wear-related industries for components such as ore crushers, pulverizing and shot-blasting equipment, liner plates, and vertical roller mill liners [11–15]. The importance of these alloys becomes evident when considering that nearly a quarter of the world's annual energy output is utilized to address tribological

challenges. In the mining and mineral industry alone, friction and wear-related malfunctions contribute to approximately 6% of the global energy usage [16,17]. Moreover, increasing friction and wear in engines and other machinery in the transportation section can result in lower fuel efficiency and higher emissions. These challenges not only have direct financial implications, but also secondary costs such as extended downtime, degraded product quality and reduced productivity [18,19].

While understanding and improving wear resistance is crucial, a fundamental aspect of this research involves studying the indentation behaviour of these alloys, which serves as a model due to their multiscale, multi-phase microstructure that effectively acts as a quasicomposite material. Contact mechanics is pivotal for understanding interactions between contacting surfaces, which is particularly relevant for indentation studies [20]. This field aids in predicting material behaviour under various loading conditions, essential for designing and evaluating materials used in various environments. Traditional contact mechanics models, such as Hertzian contact theory, are used for fully elastic contacts. However, Hertzian theory is limited as it requires perfectly smooth contacting surfaces and models a round body

E-mail address: pranav.nayak@uni-saarland.de (U.P. Nayak).

^a Department of Materials Science, Saarland University, Campus D3.3, 66123, Saarbrücken, Germany

b Materials Engineering Centre Saarland (MECS), Campus D3.3, 66123, Saarbrücken, Germany

^{*} Corresponding author.

contacting a flat body [20,21].

To address the limitations of Hertzian theory, Greenwood and Williamson (GW) developed a model that stochastically represents rough surfaces, extending the analysis to multiple sphere-on-plane contacts. The GW model considers random asperity distribution, constant radius of curvature for asperities, mechanical independence of deforming asperities, and no bulk material deformation under asperity loading [21, 22]. Statistical parameters like asperity radius, areal asperity density, and surface height standard deviation must be calculated to apply the GW model [22,23]. While suitable for purely elastic contact, the GW model is insufficient for elasto-plastic regimes, necessitating alternative models Kogut-Etsion [24], Chang-Etsion-Bogy like Zhao-Maietta-Chang [26], Shankar-Mayuram [27], and Jackson-Green [28,29].

The Jackson-Green (JG) model is advantageous because it is not reliant on limiting assumptions, such as the hardness of the material. To determine the deformation regime, the plasticity index (ψ) must be calculated [23,29,30]. This index qualitatively describes the extent of plastic deformation in the asperities on the rough surface. If the plasticity index is below 0.6, the system deforms purely elastically, whereas values above 1 indicate a plastic regime. The plasticity index serves as a critical parameter in contact mechanics, providing insights into the transition from elastic to plastic deformation [29]. By calculating the plasticity index, the behaviour of materials under varying loading conditions can be predicted, aiding in the selection of suitable models for accurate analysis [31].

While traditional models often focus solely on the softer matrix phase, this study aims to incorporate the bulk properties of the alloy, including both matrix and carbides to provide a representative understanding of indentation behaviour in multi-phase systems. Accordingly, two hypoeutectic HCCI alloys (16 % Cr and 26 % Cr) were indented using an alumina spherical ball with a custom-designed rig under various loads determined by Hertzian contact theory (HCT). Recognizing the limitations of HCT for heterogeneous microstructures, plasticity index calculations were performed using the surface characteristics derived from both matrix and carbide phases. Additionally, an image segmentation approach was employed to extract phase distribution and estimate bulk properties, enabling a probabilistic assessment of phase interaction during indentation. The main objective of the current work is to understand the indentation behaviour of HCCI alloys as a whole and to explore whether this understanding can be extended to predict their wear behaviour and applied to other multiphase materials.

2. Experimental methodology

2.1. Materials

The chemical composition of the two as-cast HCCI alloys used in this study (16 wt% Cr and 26 wt% Cr, referred to as 16 % and 26 %, respectively) was determined using optical emission spectroscopy (GNR Metal Lab 75/80; G.N.R. S.r.l., Agrate Conturbia, Novara, Italy) and is detailed in Table 1. The casting specifics are provided in Ref. [32]. Cast samples, measuring 20 mm \times 20 mm \times 10 mm were cut using an abrasive disk and then hot embedded in conductive resin for microstructural characterization. Additionally, a pure iron platelet (99.5 % purity, Goodfellow GmbH), measuring 20 mm \times 20 mm \times 1 mm was included in this study to verify the accuracy of the indentation process and eliminate the possibility of any lateral movement or slippage.

Standard metallographic procedures, as described in Ref. [33], were followed to achieve a scratch-free, mirror-polished surface.

The root mean square value $(S_q),$ was used to quantify the roughness of the polished, unetched samples, measured over an area of approximately 650 $\mu m \times$ 650 μm using a LEXT OLS 4100 Olympus confocal laser scanning microscope (CLSM) (Olympus Corporation, Tokyo, Japan). The CLSM operates at a wavelength of 405 nm, providing lateral and vertical resolutions of 120 nm and 10 nm, respectively. The pure iron platelet showed an S_q value of 0.05 \pm 0.01 μm , while the HCCI samples showed an S_q value of 0.04 \pm 0.01 μm .

Microstructural characterization of the polished surfaces was conducted using a Thermo-Fisher Helios™ G4 PFIB (Plasma Focused-Ion Beam) CXe DualBeam™ FIB/SEM, operated at an accelerating voltage of 5-15 kV and a beam current of 1.6 nA. Prior to imaging, the HCCI samples were etched with Vilellas reagent (100 mL Ethanol + 5 mL HCl + 1 g Picric Acid) for 7s. The microstructure of both HCCI alloys revealed a network of M7C3 (M: Cr, Fe) type eutectic carbides (EC) dispersed within a predominantly austenitic matrix (γ), along with a thin layer of martensite (α ') located between the EC and γ , as illustrated in the SEM micrographs in Fig. 1. Further analyses of the elemental composition and phase fraction quantification have been previously conducted and documented [32,33]. As an illustrative reference, optical micrographs of both the 16 % and 26 % Cr HCCI alloys are presented in Supplementary Fig. S1, along with WEKA-segmented and binarized images in which the carbide volume fraction and spatial distribution of EC can be visualized. The formation of martensite is attributed to the local depletion of C and Cr during the formation of EC, a well-documented phenomenon that occurs during the casting of these alloys [15,34–36]. The microstructural constituents in in this work are identified using color-coded arrows:

Austenite (γ): Red arrow pointing downwards. Martensite (α '): Green arrow pointing upwards. M_7C_3 Eutectic Carbide (EC): Yellow arrow pointing right.

2.2. Indentation testing

The indentation tests were carried out using a custom tribo-electrical testing rig on the polished, un-etched surfaces of the HCCI samples and the pure Fe sample using 3 mm diameter alumina (Al $_2$ O $_3$) balls (99.00 %–99.99 % purity; Grade GD28) as the counter-body [37]. The counter-body presented an S_q value of 0.25 \pm 0.05 μm , determined using CLSM. Prior to the indentation tests, the balls were cleaned by immersing them in an ultrasonic bath with acetone and isopropanol for 10 min each.

Although real industrial applications of HCCI alloys often involve multi-particle abrasives (e.g., silica), the intent here is not to replicate those environments in full. Instead, a single, rigid alumina sphere was chosen to provide a well-defined, high-hardness contact that isolates the fundamental load-carrying synergy between the alloy's matrix and embedded carbides. This approach offers a reproducible baseline from which more complex abrasion scenarios can later be evaluated, rather than attempting to mirror all industrial wear conditions.

The indentation load (P) was selected based on the determination of the critical load (P_c), which represents the load at which plastic deformation begins in the material. HCT was employed in determining the respective P_c for both HCCI samples using Equations (1) and (2). Furthermore, the contact radius was also estimated using HCT and it is presented in Equation (3) [38]. It is worth noting that the P_c and contact radii calculations were performed by taking into account the properties

Table 1Bulk chemical composition (wt.%) of the HCCI samples measured by optical emission spectroscopy.

	С	Cr	Mn	Ni	Mo	Si	Cu	P	S	Fe
16 % HCCI	2.43	15.84	0.76	0.18	0.41	0.47	0.04	0.02	0.02	Bal.
26 % HCCI	2.53	26.60	0.66	0.26	0.24	0.37	0.03	< 0.01	0.04	Bal.

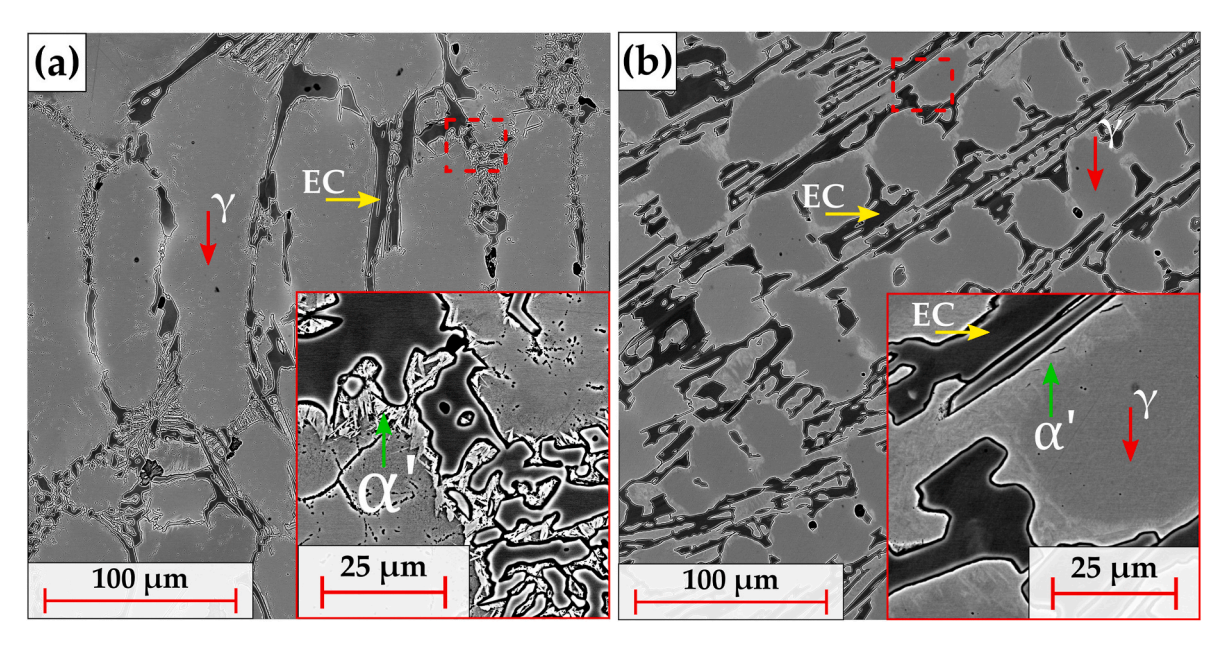


Fig. 1. (a) and (b) show SEM micrographs illustrating the microstructural constituents of 16 % and 26 % Cr HCCI alloys after Vilella etching. Phase reference: Austenite (γ), downwards red arrows; martensite (α), upwards green arrows; EC (M_7C_3), yellow arrows. Insets provide a closer look at the phase interfaces.

 Table 2

 Individual parameters used for critical load calculations.

Material	E (Pa)	H (Pa)	ν	С	S _y (Pa)	C•S _y (Pa)
Al_2O_3	3.65E11 [42]	14.1E09 [42]	0.22 [43]	1.5226	4.97E09	7.57E09
16 % matrix	2.26E11	4.75E09	0.28 [44]	1.5914	1.67E09	2.66E09
26 % matrix	2.38E11	5.60E09	0.28 [44]	1.5914	1.97E09	3.14E09
Pure Fe	2.00E11	1.47E09	0.29	1.6031	0.52E09	0.83E09

of the alumina ball and the matrix of the HCCI alloy i.e., the softer of the two phases (compared to EC).

$$P_{c}=\frac{4}{3}\bigg(\frac{R}{E}\bigg)^{2}\bigg(\frac{C}{2}\pi\cdot S_{y}\bigg)^{3} \tag{1} \label{eq:pc}$$

$$\frac{1}{E^{'}} = \frac{1-\nu_{1}^{2}}{E_{1}} + \frac{1-\nu_{2}^{2}}{E_{2}} \; \; ; \quad C = 1.295 \; exp \; (0.736 \nu) \label{eq:continuous}$$

$$a = \sqrt[3]{\frac{3 PR}{4E}} \tag{3}$$

The critical contact force at yielding (P_C, in N) was calculated using the following parameters: R is the radius of the alumina ball (m), E' is the equivalent elastic modulus (GPa), E_1 and E_2 , ν_1 and ν_2 represent the elastic modulus and Poisson's ratio of the alumina ball and the matrix, respectively. S_v denotes the yield strength of the matrix, C is the yield strength coefficient and a is the Hertzian contact radius. Hardness (H) and Young's modulus (E) of the matrix phase in the HCCI samples (GPa) were obtained through nano-indentation using a Hysitron TI 900 TriboIndenter fitted with a Berkovich tip [39]. A tip depth of 200 nm was employed in displacement mode, with a loading/unloading rate of 50, and the scan covered an area of roughly 30 μm . Each indentation test lasted for 2 min, with final values averaged from 25 measurements. The matrix yield strength was derived from the hardness using a modified Tabor relationship ($S_v = H/2.84$) [39,40]. Although a Tabor factor of 2.84 was adopted to derive the matrix yield strength (Sy) from hardness, it is acknowledged that this constraint factor can reasonably vary from about 2.80 up to 3.00 for steel-like or austenitic matrices [41]. To confirm that small deviations in the Tabor factor do not alter the conclusions, matrix Sy (and subsequent contact-mechanics parameters) was

recalculated using values of 2.80 and 3.00. Across this entire range, the resulting yield strengths, and thus the computed plasticity indices, were found to vary only minimally (within ± 7 %), remained well within the conventional 0.1–100 domain for elasto-plastic contact, and exhibited no significant effect on the overall trends. Therefore, results are presented using a value of 2.84 for clarity, while noting that the conclusions remain robust across the typical Tabor factor range of 2.8–3.0. The specific values of the parameters used in Equations (1) and (2) are provided in Table 2.

Based on the parameter input, a critical load of $\sim\!10$ N and 15 N was obtained for the 16 % Cr and 26 % Cr sample, respectively. Accordingly, an indentation load of 5 N (P < Pc) and 15 N (P \geq Pc) was selected for this study. Table 3 represents the contact radius obtained for the two different loads for the two HCCI samples.

The indentation measurements were designed in such a way that the Al_2O_3 ball would indent the desired load on the matrix. However, due to the size of the matrix region ($\sim\!50~\mu m$), targeting it specifically was a challenge. Accordingly, at least 30 indentations were carried out per load, per sample. The indentations were performed sequentially along a linear path, with the step size (200 μm) chosen to avoid any overlap in subsequent indentations.

Table 3 Hertzian contact radius for 16 % Cr and 26 % Cr HCCI alloys at 5 N and 15 N loads.

	Material	At 5 N load	At 15 N load		
•	16 % HCCI	3.35E-05 m	4.83E-05 m		
	26 % HCCI	3.32E-05 m	4.78E-05 m		

2.3. Microstructural characterization

The indentations and the surrounding microstructure were analysed using CLSM and Scanning Electron Microscopy (SEM). Post-indentation electron backscatter diffraction (EBSD) measurements were conducted using the FEI Helios $^{\rm TM}$ Nanolab 600 FE-SEM workstation equipped with an EDAX Hikari EBSD camera. The parameters included an acceleration voltage of 20 kV, a beam current of 11 nA, 5×5 binning on a hexagonal grid, and a step size ranging from 50 to 200 nm. The EBSD data was processed using the Orientation Imaging Microscopy (OIM $^{\rm TM}$ v.7) Data Analysis software from EDAX Corporation. Post-processing involved standard noise reduction techniques, such as grain confidence index (CI) standardization and grain dilation, followed by the exclusion of points with a CI below 0.1. Kernel Average Misorientation (KAM) measurements were performed within matrix regions, using 2nd neighbour KAM with a 5° threshold to ensure reliable data interpretation at the selected fine step size [45].

2.4. Wear testing

Dry-sliding linear reciprocating wear tests on the HCCI samples were performed using a ball-on-disc micro-tribometer (CSM Instruments), housed within an environmental chamber. The same alumina balls as in the indentation tests were used as the sliding counter-body. The testing was conducted under controlled conditions with a temperature of 25 $^{\circ}\mathrm{C}$ and a relative humidity of 45 %. The tests utilized loads of 5 N and 20 N, with a sliding velocity of 0.02 ms $^{-1}$ and a stroke length of 5.5 mm. Each test consisted of 2000 cycles, and data acquisition was carried out at a frequency of 50 Hz, with at least three sets of tests conducted for each sample to ensure statistical representation.

The wear rate (WR) was calculated by measuring the volume loss along each wear track using the LEXT software in the CLSM, taking the entire wear track into account, including its ends. The WR was calculated using equation (4) , where V is the wear volume (mm³), l is the total sliding distance ($5.5 \times 2 \times 2000 \text{ mm}$), P is the applied load (N) and WR is the wear rate (mm³ N⁻¹ mm⁻¹) [46].

$$WR = \frac{V}{1 \times P} \tag{4}$$

3. Results and discussion

3.1. Indentation at 5 N

When the HCCI samples were indented with a 5 N load, no visible imprint was initially observed on either alloy. To enhance the contrast and potentially reveal any subtle imprints, the samples were sputtered with an $\rm Au_{80}Pd_{20}$ coating ($\sim\!20\text{--}30$ nm thick) using physical vapor deposition. Using CLSM, the imprints on the 16 % Cr HCCI sample were successfully located, although they were barely visible. The coating greatly aided in the identification of the imprint, which is marked with a dashed circle in Fig. 2 (a). However, no imprints were observed on the 26 % Cr HCCI sample, even after sputtering. This absence of visible indentations on the 26 % Cr HCCI sample at a 5 N load suggests that no plastic deformation occurred, aligning well with the calculations of the critical load for this alloy.

Additionally, tests were conducted on a pure Fe sample to ensure the accuracy of the indentation process and rule out any potential lateral movement or slippage during indentation. The pure Fe sample, chosen for its softness, was subjected to an indentation load of 5 N, which is 50 times its calculated critical load of approximately 0.1 N. The CLSM images showed a clear, circular imprint, as represented in Fig. 2 (b). Based on the height profile, a pronounced valley was seen with the lowest point corresponding to the centre of the imprint in the contour plot. From the contour plot and the height profile, the imprint and the profile were nearly symmetrical, indicating that the indentation process was strictly perpendicular, and the spherical ball created a circular imprint without any slippage.

At a 5 N load, the imprint radius on the 16 % Cr HCCI alloy was observed to be $28.38\pm1.22~\mu m,$ which is reasonably close to the Hertzian contact radius of 33.5 μm presented in Table 3. Notably, while faint imprints were identified on the 16 % Cr alloy after sputtering, no visible imprints were detected on the 26 % Cr HCCI alloy under the same conditions. These observations prompt several questions regarding the

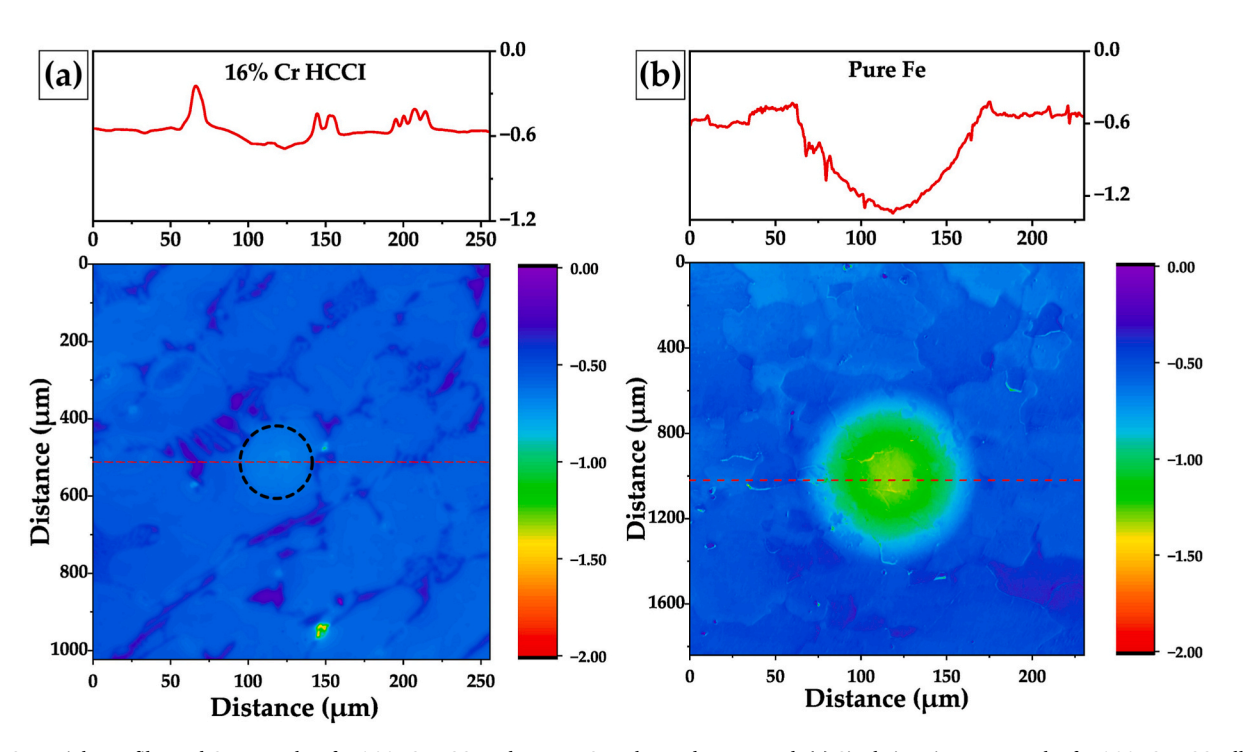


Fig. 2. CLSM Height Profiles and Contour Plots for 16 % Cr HCCI and Pure Fe Samples Under 5 N Load. (a) Single imprint contour plot for 16 % Cr HCCI alloy after sputtering with Au–Pd. (b) Single imprint contour plot for pure Fe sample.

indentation behaviour of both HCCI alloys at this load, warranting further detailed examination.

- 1. Why were faint imprints observed on the 16 % alloy but absent on the 26 % despite both alloys being subjected to a load below their respective critical loads?
- 2. What factors contribute to the discrepancy observed between the calculated and the theoretically predicted imprint radius values?

The key to understanding these results lies in the microstructural differences between the two alloys, particularly in terms of carbide volume fraction (CVF) and the spatial distribution of carbides, both of which influence the mean free path available for the indenter to interact with the matrix. The mean free path, defined as the average distance an indenter can travel across the microstructure before encountering a carbide, plays a crucial role here [47,48]. Experimentally, the CVF was determined to be approximately 20 % for the 16 % Cr alloy and 30 % for the 26 % Cr alloy [32]. The higher CVF in the 26 % Cr alloy leads to a denser carbide configuration, thereby reducing the mean free path and limiting the indenter's ability to compress the matrix directly at lower loads, as demonstrated in the micrographs presented in Fig. 1. This microstructural arrangement effectively shields the matrix from the indenter's force at low loads, which is evident from the absence of imprints at 5 N in the 26 % Cr alloy. In contrast, the 16 % Cr alloy, with its comparatively lower CVF and larger mean free path, allows the indenter to reach and deform the matrix even at lower loads, as suggested by the visible imprints after sputtering. This is illustrated in the schematic diagram in Fig. 3 where the indenter in the 16 % alloy is more likely to depress into the matrix between carbide peaks, which are not as closely spaced as in the 26 % alloy.

The presence of faint imprints on the 16 % Cr HCCI sample at a load of 5 N, which is below its theoretically calculated critical load of 10 N, might initially seem contradictory. One possible explanation is the local variability in carbide distribution and the resultant matrix areas exposed to the indenter. While the critical load calculations assume a uniform stress distribution across a homogenous matrix surface, actual microstructural conditions may present localized regions where the matrix is more exposed or less shielded by carbides. In the 16 % Cr alloy, the larger mean free path and lower CVF result in regions of exposed matrix that are more susceptible to deformation under lower loads. Additionally, the impact of load distribution and stress concentration around the

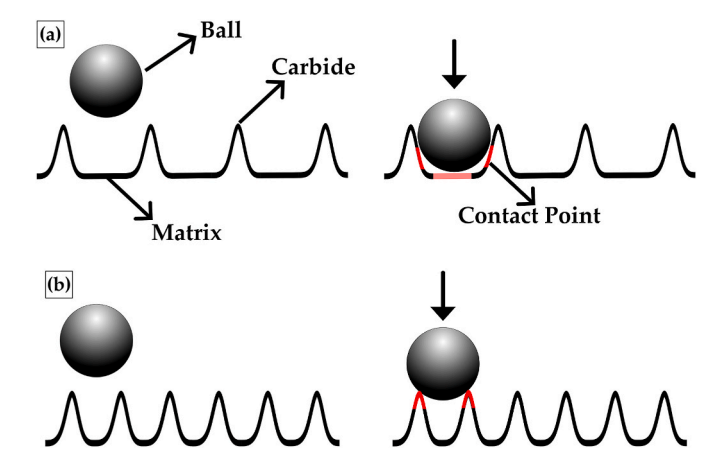


Fig. 3. Schematic representation of the indentation process in (a) 16 % HCCI alloy and (b) 26 % HCCI alloy at 5 N. The left images in both panels depict the microstructural profile prior to indentation, highlighting the carbides (peaks) and matrix (flat areas). The right images demonstrate the post-contact scenario, where the red highlighted areas indicate potential points of contact with the indenter. This visual illustrates the higher 'mean free path' in the 16 % alloy, facilitating more probabilistic indenter-matrix interactions, compared to the 26 % HCCI alloy.

carbides might also play a significant role. Even under a load below the calculated critical value, the stress might not be uniformly distributed across the indented area. Stress concentration at the edges of carbides or at weak spots in the matrix could lead to localized deformation, making faint imprints detectable. Moreover, the inherent roughness of the counterbody may further contribute to localized deformation, as the asperities of the ball contact the softer matrix.

The slight discrepancy between the calculated and theoretically predicted imprint radius highlights the limitations of traditional critical load calculations that primarily consider the matrix's properties in isolation. In reality, the indentation process in a multi-phase material like HCCI does not solely engage the matrix but also interacts with the dispersed carbides. This results in a reduced imprint radius compared to the matrix-based prediction. Nonetheless, the observed imprint radius is in good agreement with the value predicted by HCT.

Further implications of these observations will be discussed in Section 3.4, Load-bearing Capacity and Wear Performance, where the performance of both alloys under higher loads is examined. The comparison will also tie back to these initial findings, providing a comprehensive understanding of how microstructural characteristics influence mechanical behaviours under varying stress conditions.

3.2. Indentation at 15 N

Fig. 4 represents the contour plots and height profiles of the $16\,\%$ and $26\,\%$ Cr HCCI alloys under a $15\,$ N normal load, illustrating the differences in topography and indentation behaviour. The contour plots were created using a matrix of height data, with a horizontal line representing the height profile at a specific line passing through all indents providing detailed insights into the surface characteristics.

For both the 16 % and 26 % Cr HCCI alloys, the height profiles reveal significant variations with pronounced peaks and valleys, where the depth of the valleys reaches approximately $-1.0~\mu m$. The overall roughness appears higher in the 26 % Cr HCCI alloy, indicated by more pronounced peaks and slightly deeper valleys in the contour plots. The corresponding colour maps highlight regions with high and low elevations, suggesting a heterogeneous surface with substantial local height variations for both alloys, although these variations are more pronounced in the 26 % Cr HCCI alloy. This behaviour is observed as a result of the higher number of carbides present in the 26 % Cr HCCI alloy. Conversely, the 16 % Cr HCCI alloy displays a smoother surface with less severe topographical variations.

The imprint radius changes depending on whether the indenter contacts an area that is primarily comprised of carbides or primarily of the matrix. When the indenter interacts more with a carbide-rich area, the imprint radius is lower, as carbides are harder and less deformable compared to the matrix. This is clearly visible by observing imprint 3 and 4 in Fig. 4(a) and (b). The height profiles show that the carbides protrude higher than the matrix, meaning that the first asperity encountered during indentation is often an outstanding carbide. Since the predicted contact radius is similar to the matrix area, it is not possible to only indent the matrix, and the indentation inevitably involves carbides.

Higher magnification images of single imprint micrographs for both alloys (Fig. 4(c) and (d)) provide further insights into the interaction between the indenter and the carbide/matrix system with the peaks (representing carbides) and valleys (representing the matrix) becoming more pronounced under indentation. Considering the austenitic nature of the matrix, its ability to plastically deform around the carbides plays a critical role in maintaining the overall structural integrity and loadbearing capacity of the material. Furthermore, the carbides within the indentation retain a visible height profile, although lower than the unindented carbides. This indicates that the carbides are pushed into the matrix rather than fractured. This phenomenon is clearly illustrated in Fig. 4 (c) and 4 (d) where the height profiles of both indented and unindented carbides are highlighted using a grey square. Despite the

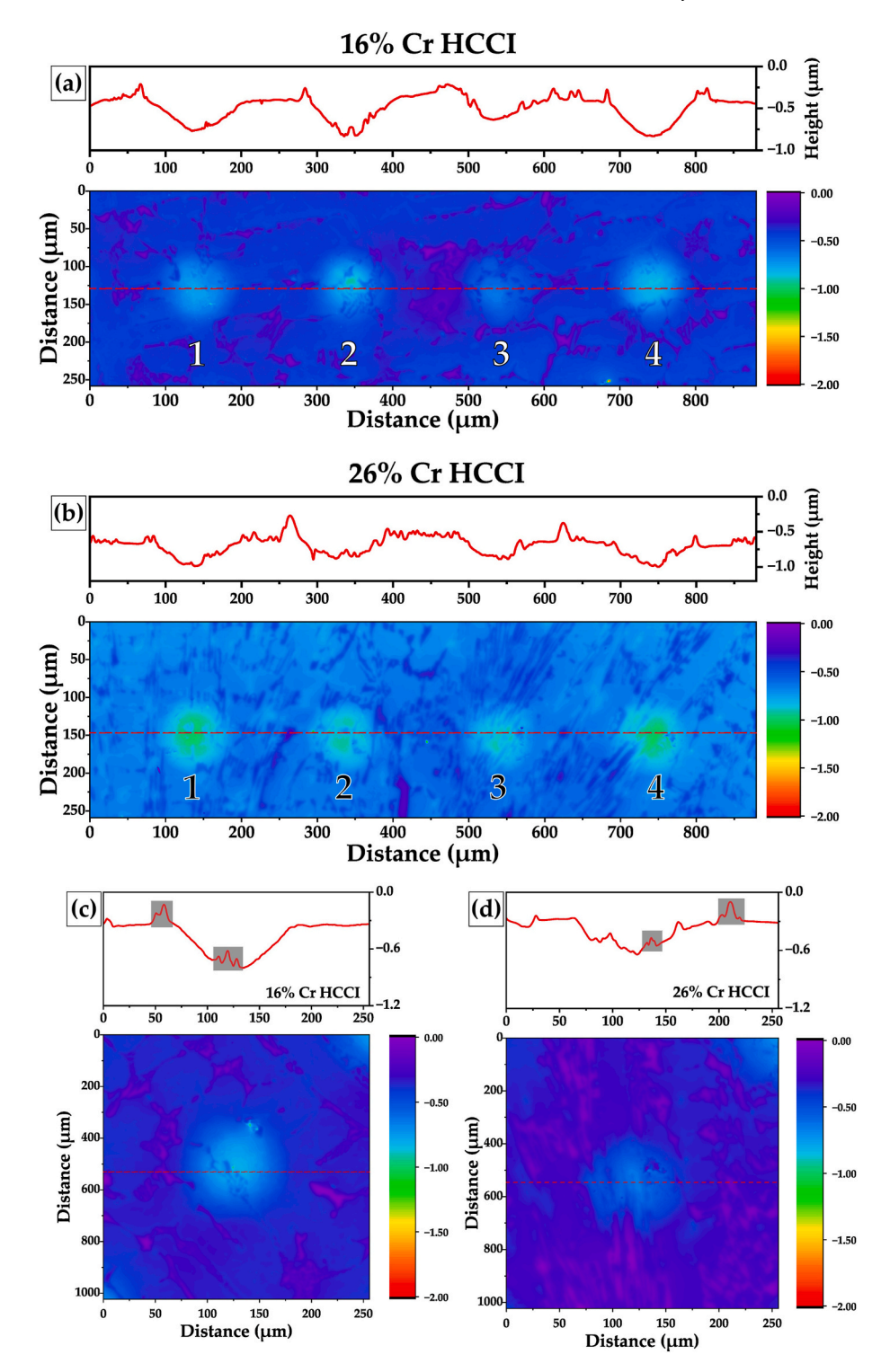


Fig. 4. CLSM Height Profiles and Contour Plots for 16 % and 26 % Cr HCCI Alloys Under 15 N Load. (a) and (b) 4 imprint contour plots for 16 % and 26 % Cr HCCI alloy, respectively. (c) and (d) Single imprint at higher magnification (50X) for 16 % and 26 % Cr HCCI alloy, respectively.

absolute height difference, the carbides continue to protrude from the matrix, demonstrating that the indentation process displaces the carbides into the matrix without causing them to crack. This behaviour is facilitated by the slow indentation speed, which allows the matrix to deform plastically and absorb the energy, preventing carbide cracking. Moreover, the austenite-martensite-carbide gradient further aids energy absorption and optimizes load transfer, effectively preventing interfacial detachment.

The average imprint radius for the 16 % Cr HCCI alloy was calculated

to be $49.93\pm2.03~\mu m$, whereas for the 26 % Cr HCCI alloy it was $49.55\pm1.43~\mu m$. These values are comparable, although the 16 % Cr HCCI alloy showed a slightly higher average, which is also in accordance with the values predicted via HCT (Table 3). Despite minor differences, the overall agreement between experimental and theoretical values for both alloys underscores the reliability of the contact mechanics models used in this study.

Further insights into the microstructural response to indentation were obtained from SEM micrographs of the $16\,\%$ and $26\,\%$ Cr HCCI

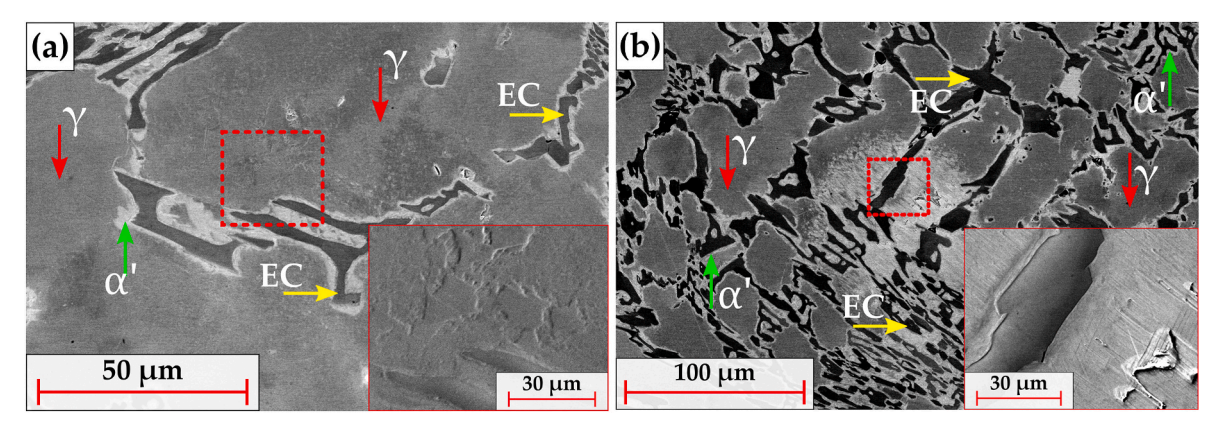


Fig. 5. BSE SEM images of 16 % Cr HCCI alloy (left) and 26 % Cr HCCI alloy (right) subjected to a 15 N load. The insets show higher magnification secondary electron images indicating the plastic deformation of the matrix while the carbides remain intact. The various microstructural constituents are colour-arrow coded for reference.

alloys subjected to a 15 N load, captured in both backscattered electron (BSE) and secondary electron (SE) modes, presented in Fig. 5. The SEM micrographs focus on the area around a single imprint, revealing crucial details about the interaction between the indenter and the HCCI microstructure.

In the BSE SEM micrographs of both alloys, it is clear that the carbides remain intact without any signs of cracking under the 15 N load applied during testing. The higher magnification SE images provide detailed insights, particularly highlighting the plastic deformation of the austenitic matrix. The flow lines observed around the matrix regions are a clear indicator of matrix deformation, specifically where it blankets over the edges of the carbides, indicating a crucial material response to the indentation.

The interplay between the behaviour of the carbides and the matrix during deformation is key. The carbides, being the initial point of contact with the indenter, bear the brunt of the applied load and transfers it to the surrounding matrix [39,49]. The austenitic matrix, characterized by its ductility, not only supports the carbides but also undergoes plastic deformation, effectively absorbing and redistributing the applied stress [50]. This capability of the matrix to absorb energy and allow for material flow under stress ensures that the hard carbides remain intact, thereby enhancing the alloy's load-bearing capacity and potentially its wear resistance [51,52]. This behaviour, facilitated by the slow indentation speed, prevents cracking and failure of the carbides, highlighting the importance of matrix properties in the performance of HCCI alloys. These SEM observations depict the critical role of the matrix in maintaining the structural integrity of HCCI alloys under indentation.

The EBSD maps presented in Fig. 6 provide a deeper understanding of the microstructural changes taking place at the crystallographic level. The 26 % alloy indented at 15 N is used as an exemplar. The image quality (Fig. 6 (a)) and phase map (Fig. 6 (b)) clearly outline the imprint region and highlight the significant deformation in the matrix, especially around the EC, where some regions could not be indexed due to poor Kikuchi pattern quality, commonly observed at phase boundaries or in highly strained areas. The grain reference orientation deviation map of the entire sample depicted in Fig. 6 (c) illustrates the increased misorientation in the indented carbides and their surrounding matrix compared to the less affected regions further from the imprint. The colour gradient highlights areas of higher misorientation, indicating significant local changes in orientation within the matrix close to the indentation. This is corroborated by the close-up kernel average misorientation map of the austenitic matrix presented in Fig. 6 (d), which shows elevated misorientation near the carbides, suggesting effective load transfer from the carbides to the matrix during the initial stages of indentation. Additionally, the inverse pole figure maps (Fig. 6 (e)) show that the crystallographic orientation of the carbide and especially the matrix largely remain unchanged, even under direct

indentation. Notably, no carbide cracking or strain-induced martensite (SIM) formation was observed, which can be attributed to the low strain rate and the absence of lateral shearing movements that are typically necessary for generating shear band intersections, critical nucleation sites for SIM formation [53–55].

Furthermore, in addressing the observed plastic deformation of the 26 % Cr HCCI alloy indented at 15 N,a load equal to its calculated critical load, it is crucial to highlight the importance of considering the bulk properties of the alloy. Typically, the critical load calculations are based on the matrix properties alone, but such an approach does not account for the simultaneous impact on both the matrix and the carbides during indentation. This necessitates incorporating bulk hardness into the analysis. For the 26 % Cr alloy, the Rockwell C hardness was measured at 49.3, corresponding to an equivalent hardness of 4.93 GPa [56]. When recalculated with this bulk hardness, the critical load is adjusted to 10.3 N, clarifying why significant plastic deformation and clear imprints were observed at a 15 N indentation load. This adjustment demonstrates the importance of accounting for bulk hardness in order to accurately assess the material's mechanical response under applied loads.

3.3. Contact mechanics calculations

Although, HCT offers a foundational understanding of the contact mechanics between smooth, elastic bodies, its applicability is limited when dealing with real surfaces, where asperities and topographic features (e.g., outstanding carbides) play a significant role in the contact behaviour. The GW model was developed to overcome certain limitations of HCT. Greenwood and Williamson introduced a statistical approach to model the contact between rough surfaces by assuming that the asperities of a given surface could be modelled as a collection of spherical caps with a Gaussian distribution of heights [21,30]. This approach allowed for a more realistic representation of surface contact compared to earlier models that assumed perfectly smooth surfaces. For more realistic scenarios, the calculation of the plasticity index (PI) becomes crucial. The PI provides a measure of the extent to which a material will undergo plastic deformation under contact pressure. Prior to determining the PI, statistical surface parameters must be determined (i. e., spectral moments), which can be obtained directly from surface topography measurements acquired via CLSM. As described by McCool et al. [22,28], the spectral moments can be used to determine the standard deviation of the surface heights (σ_s), the areal asperity density $(\eta),$ and the radius of curvature (r). Subsequently, the McCool parameters can be employed to determine the standard deviation of asperity heights (σ_a) [57], as well as the critical interference as derived by Jackson and Green [58,59]. These two parameters are then combined to determine the PI [29,57]. Furthermore, the individual asperity contact

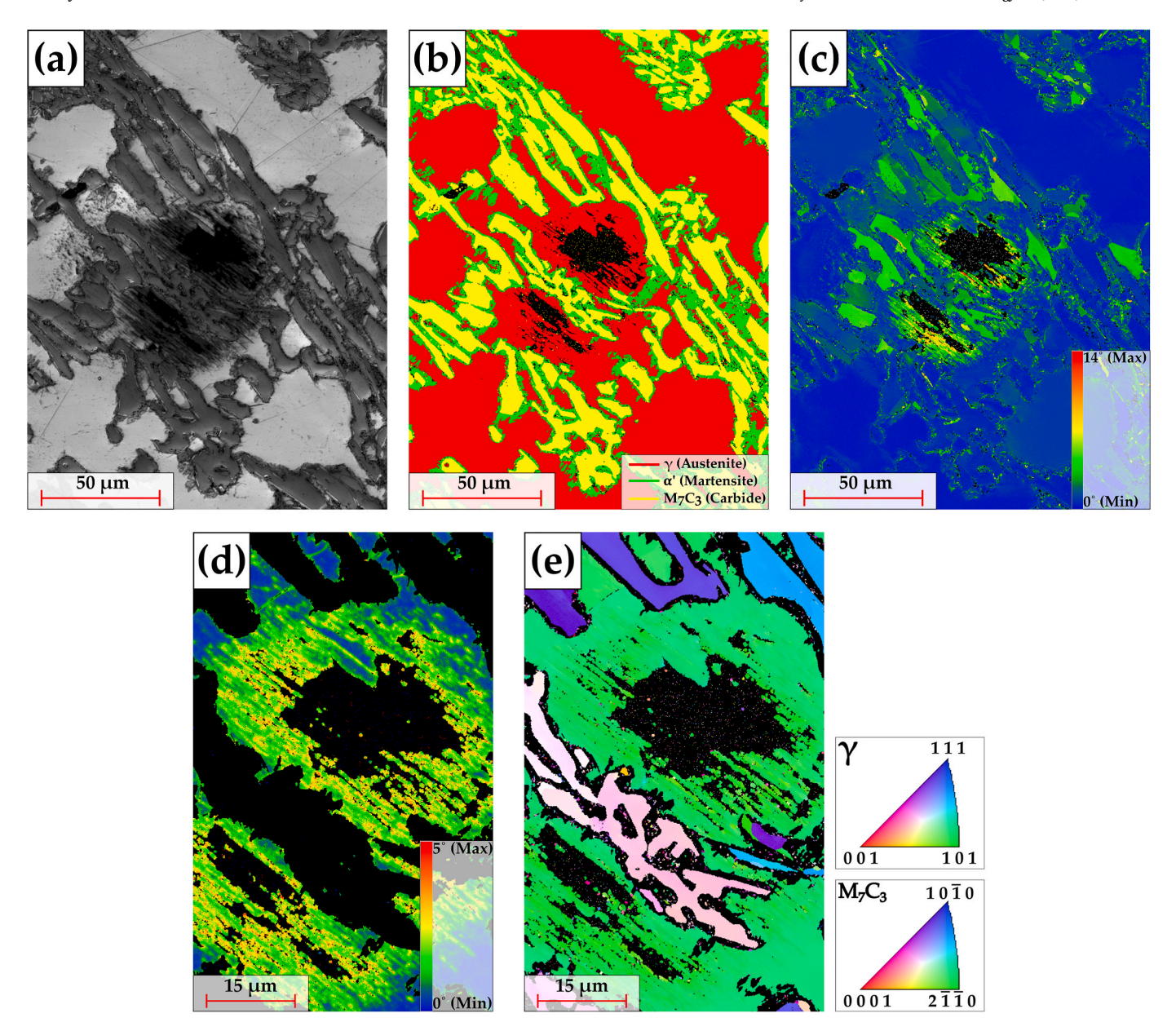


Fig. 6. EBSD analysis of the 26 % Cr HCCI alloy subjected to 15 N indentation load: (a) Image Quality Map showing regions of significant deformation, (b) Phase Map, (c) Grain Reference Orientation Deviation Map illustrating the misorientation surrounding the indented carbides, (d) Close-up of the matrix with the Kernel Average Misorientation Map and (e) Inverse Pole Figure Maps of the austenitic matrix and the M₇C₃ EC.

force and area of contact can be determined via the equations provided by Jackson and Green [29]. Further detailed information on this procedure can be found in Refs. [23,28,29,58–60].

The PI is mathematically defined as the square root of the quotient between the standard deviation of asperity height and the critical interference. The former physically represents the height of outstanding asperities, whereas the latter is the degree to which an asperity must deform for the onset of plasticity to occur. In other words, the critical interference indicates the maximum elastic deformation that an asperity can endure prior to plastic deformation. Analogously, the critical load and area are defined as the minimum load or contact area required for an asperity to plastically deform. The critical parameters (load, area, and interference) of individual asperities can also be determined, as described by Jackson and Green [29,59]. However, these were not calculated since the focus of the work herein reported is primarily on determining the PI and correlating its numerical calculation with wear performance of the multi-phase alloy.

As previously discussed, and as can be observed in Figs. 4 and 5, it is not possible to indent only the matrix region of the HCCI alloy. The heterogeneous nature of the HCCI alloy, with dispersed carbides within the matrix, posed challenges in isolating the matrix during indentation. Furthermore, the spectral moments used in these calculations considered the entire CLSM micrograph, which includes both matrix and carbide phases. Therefore, an alternative approach was employed to account for both the matrix and the carbides in the calculation of the PI.

Analytical Procedure for Plasticity Index Calculation.

Initial Contact Radius Calculation:

As an initial approach, the elastic modulus (E) and Poisson's ratio (ν) of the alumina ball and the matrix of HCCI were used to estimate the Hertzian contact radius for the two loads for both HCCI alloys, as shown in Table 3.

Table 4
Comparison of carbide volume fraction (CVF) and carbide size in 16 % and 26 % HCCI alloy.

Sample	Mean CVF in Bulk (Entire micrographs) [32] (%)	Mean CVF in 7×7 Split (3 images) (%)	Median CVF in 7 × 7 Split (3 images) (%)	Mean Avg. Size in 7 \times 7 Split (3 images) (μm^2)	Median Avg. Size in 7 \times 7 Split (3 images) (μm^2)
16 % HCCI	19.4 ± 0.4	19.04 ± 4.36	18.85	88 ± 34	80
26 % HCCI	30.4 ± 0.6	30.09 ± 4.35	29.5	137 ± 57	130

Projection and Equivalent Square Calculation:

Given the spherical nature of the indentation, the projected area is circular. From the obtained contact radius (r), the equivalent side length (a) of a square with the same area was calculated using Equation (5):

$$\pi r^2 = a^2 \Rightarrow a = \sqrt{\pi} r \tag{5}$$

As an exemplar, at 15 N the indentation on the 26 % HCCI matrix would yield a radius of 47.79 μm (shown in Table 3) and the equivalent side length of the square was determined to be 84.71 μm .

Image Trimming and Statistical Analysis Using ImageJ:

Using the calculated side length as the trimming window dimensions, we determined the number of images that could be trimmed from the CLSM image at a magnification of $200\times$. The CLSM image dimensions were 640 $\mu m \times$ 640 μm , allowing for the extraction of approximately 7 smaller images (84.71 μm x 7 = 593 μm) from each side for a total of 49 split images per micrograph. The splitting and trimming of images were performed from the centre to maintain consistency. ImageJ software (ver. 1.54f) was used for this purpose [61], and a macro code was developed to facilitate faster batch processing. For both 16 % and 26 % Cr HCCI samples, three large CLSM micrographs were used, resulting in a total of 147 smaller images analysed for statistical representation.

Carbide Area Fraction Calculation:

For each trimmed image, the area fraction of the carbide phase was calculated, and this process was repeated for multiple micrographs to ensure statistical representation. The average area fraction of carbide was then used to determine the probability of encountering carbide within the indentation area.

Combined Elastic Modulus Calculation:

Using the obtained carbide area fraction, the combined elastic modulus of the HCCI alloy was calculated by applying the rule of mixtures:

$$E_{HCCI} = V_M E_M + V_C E_C$$

Where E_{HCCI} , E_M , and E_C represent the elastic modulus of the HCCI alloy, the matrix and the carbide, respectively. V_M and V_C are the volume fraction of the matrix and carbide, respectively. The matrix phase in this context refers to both the predominant austenitic matrix and the thin interfacial martensitic regions, with the latter not treated separately but included within the overall matrix fraction. This is due to the martensite's low volume fraction, limited spatial extent, and elastic modulus comparable to austenite, rendering its influence on the overall composite modulus negligible.

Effective Elastic Moduli and Plasticity Index Calculation:

The combined elastic modulus (E_{HCCI}) was then used with the alumina ball's properties to determine the updated effective elastic moduli, which were used to calculate the "real" plasticity index.

Although the values did not vary significantly, the approach ensured a more accurate representation of the real plasticity index by incorporating the combined elastic modulus and bulk hardness of HCCI. The plasticity index for the 16 % Cr HCCI sample was calculated to be 28.86

 \pm 0.31, and for the 26 % Cr HCCI sample, it was 28.48 \pm 0.16. These similar plasticity indices indicate that both materials exhibit comparable resistance to plastic deformation. Table 4 summarizes the CVF and size determined from the split micrographs, including mean and median values. Additionally, the CVF determined using the bulk micrograph taken from Ref. [32] is included.

The table presents the mean and median values of CVF in bulk micrographs and split micrographs, along with the average and median sizes of ECs in 16 % and 26 % HCCI alloy. Despite splitting the images for analysis, the CVF between the bulk micrograph and the split micrographs remained consistent in both the 16 % and 26 % HCCI alloy. Furthermore, it was observed that 26 % HCCI alloy exhibited a larger median carbide size (130 µm²) compared to the 16 % HCCI alloy (80 μm²). Additionally, the 26 % HCCI alloy displayed a higher carbide volume fraction (30.09 %) relative to the 16 % HCCI alloy (19.04 %). Higher chromium content HCCI has been shown to significantly influence the formation and characteristics of ECs. The presence of increased chromium content promotes the growth of larger and more stable carbides, such as M₇C₃ [62-65]. Despite these differences, the standard deviation of the carbide volume fraction remained similar for both alloys (± 4.35 for 26 % HCCI and ± 4.36 for 16 % HCCI), indicating comparable homogeneity in the dispersion of carbides within the matrix. This distribution suggests that both alloys possess a consistent microstructural framework.

Combining these observations, it can be inferred that while the $26\,\%$ HCCI alloy benefits from larger and more abundant carbides due to the higher chromium content, the similar homogeneity in carbide dispersion between the two alloys ensures that the $16\,\%$ HCCI alloy, despite having a lower carbide volume fraction and smaller carbide size, maintains a comparable load-bearing capacity. This inference will be further explored through the Abbott-Firestone curve analysis in the next section, providing insights into the wear behaviour of both alloys.

3.4. Load-bearing Capacity and Wear Performance

The Abbott-Firestone (AF) curve, also known as the bearing area curve, is a crucial analytical tool used to evaluate the load-bearing capability and surface characteristics of materials [66,67]. This curve provides detailed insights into the distribution of surface heights and helps in understanding how a material will perform under various loading conditions [68,69]. To better understand the potential wear behaviour of the 16 % Cr and 26 % Cr alloys, the AF curves were analysed based on the respective CLSM micrographs.

The combined AF curve comparison between both the alloys, shown in Fig. 7, highlights distinct differences in load-bearing capability across various bearing ratios. The graph includes three distinct regions, demarcated by the vertical dashed lines at 18 % and 95 % material ratios, and filled with light yellow (0 %–18 %), light green (18 %–95 %), and light grey (95 %–100 %). The demarcation values were chosen based on the point of inflection in the individual AF curves, with 18 % for $M_{\rm r1}$ (the first significant material ratio indicating initial contact

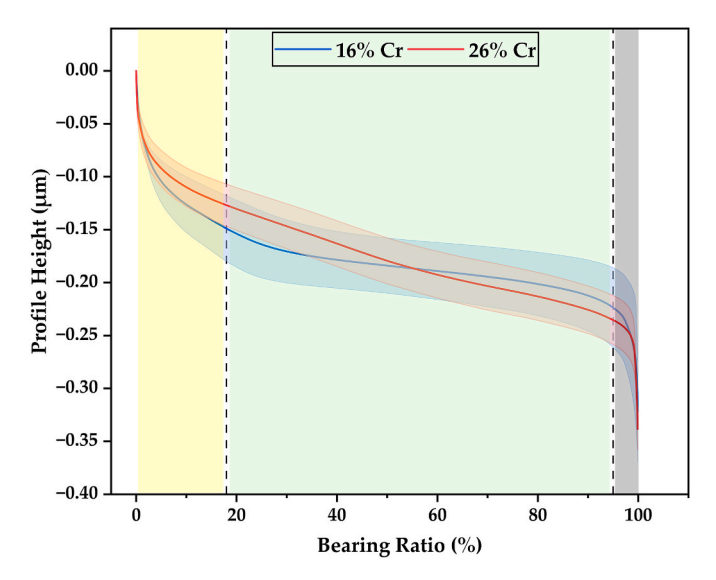


Fig. 7. Comparison of Abott-Firestone (AF) curves for 16 % Cr and 26 % Cr alloys, showing profile height (μ m) versus bearing ratio (%). The graph is divided into three regions: 0 %–18 % (initial contact phase), 18 %–95 % (steady-state load-bearing phase), and 95 %–100 %.

phase change) of 26 % Cr and 95 % for $\rm M_{r2}$ (the second material ratio marking the transition to maximum load-bearing capacity) of 26 % Cr to capture the most significant variations in material ratio. The 26 % Cr values were chosen over the 16 % Cr values due to their greater representation of the curve's inflection points, providing a clearer demarcation for analysis. The individual AF curves, providing detailed insights, are included in the supplementary information (Fig. S2).

The initial region (0 %–18 %), represents the initial contact phase. Here, both alloys show a rapid decrease in profile height, with the 26 % alloy exhibiting a slightly higher profile height than the 16 % alloy, suggesting a better load distribution in the initial contact phase. The middle region (18 %-95 %), represents the steady-state load-bearing region. Both alloys show a similar trend in this mid-range, but 26 % alloy maintains a slightly higher value than 16 % alloy, suggesting a marginally better load-bearing capacity in this range. Beyond the 95 % material ratio, the curves level off, indicating that they have reached their maximum load-bearing capacity. The differences between the two alloys diminish at this stage, showing that they perform similarly under high load conditions. The shaded regions around the curves represent measurement variability, which is comparable for both alloys, indicating consistent behaviour in their load-bearing capacities, suggesting that either alloy could be suitable depending on specific application requirements.

Following this, the WR (mm³•N⁻¹•mm⁻¹) of the two different HCCI alloys were evaluated under loads of 5 N and 20 N. The average wear volume (mm³) calculated using the LEXT software and the wear rate, computed using Eq. (4), for each load is presented in Table 5. Expectedly, the wear volume and consequently, the wear rate increased with increasing load.

The 26 % Cr alloy demonstrates slightly better wear resistance than the 16 % Cr alloy under low load conditions. However, at higher loads,

Table 5 Wear Rates (WR) (in mm 3 N $^{-1}$ mm $^{-1}$) of 16 % Cr and 26 % Cr HCCI Alloys under different loads.

Sample	Load	WR $(mm^3 \bullet N^{-1} \bullet mm^{-1})$
16 % HCCI	5	0.013 ± 0
	20	0.025 ± 0.004
26 % HCCI	5	0.010 ± 0.001
	20	0.019 ± 0.004

both alloys perform similarly when considering their wear rates and standard deviations. The similarities in the wear rates of the 16 % and 26 % Cr HCCI alloys can be attributed to several factors. Firstly, the dispersion of carbides in both alloys, as indicated by the standard deviation of the segmented images, is quite uniform. Despite the 26 % Cr HCCI alloy having a higher CVF and larger carbide size, the homogeneous distribution of carbides in both alloys results in similar load-bearing capacities. This uniformity in carbide dispersion ensures that the stress distribution within the matrix is consistent, leading to comparable mechanical responses under load.

Secondly, the similarity in the load-bearing capacity contributes to the comparable plasticity indices of both alloys. The plasticity index, calculated based on bulk properties, reflects the material's resistance to plastic deformation. The nearly identical plasticity indices for the 16 % (28.86 \pm 0.31) and 26 % (28.48 \pm 0.16) Cr HCCI alloys indicate that both materials exhibit similar resistance to plastic deformation, which directly influences their wear behaviour.

Finally, the AF curve behaviour at higher loads, particularly in the steady-state load-bearing region and beyond, shows striking similarities between the two alloys. This indicates that both alloys have similar surface profiles and load-bearing capabilities when subjected to high stresses. The consistent load-bearing performance, combined with the aforementioned factors, leads to the observed similarity in wear rates at higher loads. This suggests that while 26 % Cr alloy may offer advantages at lower stresses, both materials can be expected to perform equivalently under higher load conditions, providing flexibility in choosing either alloy based on specific application requirements.

Efforts to enhance wear resistance often focus on increasing the CVF of eutectic or primary carbides. However, this study highlights that the effectiveness of these efforts may be limited if the distribution and interplay between the carbides and the matrix are not optimal. Despite the 16 % Cr alloy possessing lower CVF and carbide size, the distribution and synergistic interaction between the carbides and the austenitic matrix contribute significantly to its load-bearing capacity, mirroring the performance of the 26 % Cr alloy under higher loads. This demonstrates the crucial role of not only the CVF but also their distribution and interaction with the matrix in determining the material's wear behaviour. Furthermore, these findings emphasize the importance of considering bulk properties, microstructural characteristics, and surface attributes in understanding material behaviour during indentation and predicting wear performance, offering valuable insights for the application of these materials in various environments.

4. Conclusions

This study investigated the indentation behaviour and wear performance of 16 % and 26 % Cr HCCI alloys. Hertzian contact theory was used to predict critical loads and contact radii, which were experimentally validated. At a 5 N load, the 16 % Cr HCCI alloy showed barely visible imprints identified via CLSM after Au–Pd sputtering, whereas the 26 % Cr HCCI alloy showed no imprints, indicating a higher critical load. Pure Fe samples confirmed the accuracy and perpendicularity of the indentation process. Additionally, at 15 N, significant topographical variations were observed, with carbides affecting the imprint radius.

Despite the lower carbide size and the volume fraction in the 16 % Cr HCCI alloy, the similarities in the dispersion of carbides in both alloys led to comparable load-bearing capacities. The plasticity index calculated using bulk properties derived from image segmentation, alongside Abbott-Firestone analysis, aligned with the observed wear behaviour. Measurements showed that while the 26 % Cr alloy performed slightly better at lower loads, both alloys exhibited statistically similar wear rates at higher loads. Overall, both alloys perform similarly under dry conditions; however, the 16 % Cr alloy could be the more economical choice due to its lower chromium content, reducing raw material demand and cost.

CRediT authorship contribution statement

U. Pranav Nayak: Writing – original draft, Visualization, Investigation, Formal analysis, Validation, Conceptualization. Bruno Alderete: Writing – original draft, Methodology, Investigation, Formal analysis. Sebastian Suarez: Writing – review & editing, Conceptualization, Formal analysis. María Agustina Guitar: Writing – review & editing, Supervision, Funding acquisition. Frank Mücklich: Writing – review & editing, Supervision, Funding acquisition, Resources.

Data and code availability

The data used in this study are available from the corresponding author at reasonable request. The associated ImageJ macro code to automate the processing and quantitative analysis of SEM micrographs by splitting them into smaller segments, and its documentation are publicly available in the Zenodo repository (https://doi.org/10.5 281/zenodo.13355380). This includes the macro script in both ImageJ format and plain text, alongside a description and usage guide detailing the operation and application of the macro for automated image processing.

Ethical approval

Not Applicable.

Declaration of competing interest

The authors declare that they have no known competing financial interests or personal relationships that could have appeared to influence the work reported in this paper.

Acknowledgement

The present work is supported by funding from the Deutsche Forschungsgemeinschaft (DFG, project: GU 2102/2-1). B. Alderete wishes to acknowledge the support from the German Academic Exchange Service (DAAD) and the Roberto Rocca Education Program (RREP). Moreover, the funding for the PFIB/SEM instrument by DFG is greatly acknowledged (INST 256/510-1 FUGG). The authors would also like to thank Martin Duarte from Tubacero S.A. for providing the materials.

Appendix A. Supplementary data

Supplementary data to this article can be found online at https://doi.org/10.1016/j.jmrt.2025.07.020.

References

- [1] Laird G, Gundlach R, Rohrig K. Abrasion resistant cast iron Handbook. Illinois: American Foundry Society, Schaumburg; 2000.
- [2] ASM International. ASM Handbook volume 15 casting. Ohio: ASM International; 2008. https://doi.org/10.31399/asm.hb.v15.9781627081870.
- [3] ASTM International. Standard Specification for abrasion resistance cast irons. West Conshohocken, PA, USA: ASTM Standard A 532/A 532M - 93a; 2003. www.astm.
- [4] Rivlin VG. Critical review of constitution of carbon chromium iron and carbon — iron — manganese systems. Int Met Rev 1984;29:299–328. https://doi. org/10.1179/imtr.1984.29.1.299.
- [5] Dodd J. Recent developments in abrasion resistant high chromium-molybdenum irons, low-alloy manganese steels and alloyed nodular irons of importance in the extraction and utilization of energy resources. J Mater Energy Syst 1980;2:65–76. https://doi.org/10.1007/BF02833432.
- [6] Durman RW. Progress in abrasion-resistant materials for use in comminution processes. Int J Miner Process 1988;22:381–99. https://doi.org/10.1016/0301-7516(88)90074-9
- [7] Maratray F. Choice of appropriate compositions for chromium-molybdenum white irons. AFS Trans 1971;79:121–4.
- [8] Wiengmoon A. Carbides in high chromium cast irons. Naresuan University Engineering Journal 2011;6:64–70. https://doi.org/10.14456/nuej.2011.6.

- [9] Doğan ÖN, Hawk JA. Effect of carbide orientation on abrasion of high Cr white cast iron. Wear 1995;189:136–42. https://doi.org/10.1016/0043-1648(95)06682-9.
- [10] Nayak UP. Interplay between the microstructure and tribological performance in heat-treated high chromium cast iron alloys. Saarland University; 2023. https://doi.org/10.22028/D291-40546. PhD Thesis.
- [11] Asensio J, Pero-Sanz JA, Verdeja JI. Microstructure selection criteria for cast irons with more than 10 wt.% chromium for wear applications. Mater Char 2002;49: 83–93. https://doi.org/10.1016/S1044-5803(02)00260-7.
- [12] Karantzalis E, Lekatou A, Mavros H. Microstructure and properties of high chromium cast irons: effect of heat treatments and alloying additions. Int J Cast Metals Res 2009;22:448–56. https://doi.org/10.1179/174313309X436637.
- [13] Tabrett CP, Sare IR, Ghomashchi MR. Microstructure-property relationships in high chromium white iron alloys. Int Mater Rev 1996;41:59–82. https://doi.org/ 10.1179/095066096790326075.
- [14] Llewellyn RJ, Yick SK, Dolman KF. Scouring erosion resistance of metallic materials used in slurry pump service. Wear 2004;256:592–9. https://doi.org/ 10.1016/j.wear.2003.10.002.
- [15] Maratray F, Usseglio-Nanot R. Factors affecting the structure of chromium and chromium-molybdenum white irons. Climax Molybdenum S A 1971:1–32.
- [16] Holmberg K, Erdemir A. Influence of tribology on global energy consumption, costs and emissions. Friction 2017;5:263–84. https://doi.org/10.1007/s40544-017-0183-5.
- [17] Holmberg K, Kivikytö-Reponen P, Härkisaari P, Valtonen K, Erdemir A. Global energy consumption due to friction and wear in the mining industry. Tribol Int 2017;115:116–39. https://doi.org/10.1016/j.triboint.2017.05.010.
- [18] Hutchings IM. Abrasion in wear and manufacturing processes. Proc IME J J Eng Tribol 2002;216:55–62. https://doi.org/10.1243/1350650021543898.
- [19] Nayak UP, Mücklich F, Guitar MA. Interplay between the microstructure and tribological performance of a destabilized 26 wt% Cr HCCI: the influence of temperature and heating rate. Tribol Int 2023;185:108532. https://doi.org/ 10.1016/j.triboint.2023.108532.
- [20] Fischer-Cripps AC. Introduction to contact mechanics. second ed. Springer US; 2007. https://doi.org/10.1007/978-0-387-68188-7.
- [21] Greenwood JA, Tripp JH. The contact of two nominally flat rough surfaces. Proc Inst Mech Eng 1970;185:625–33. https://doi.org/10.1243/PIME_PROC_1970_185_ 069_02.
- [22] McCool JI. Relating profile instrument measurements to the Functional performance of rough surfaces. J Tribol 1987;109:264–70. https://doi.org/ 10.1115/1.3261349.
- [23] Reinert L, Green I, Gimmler S, Lechthaler B, Mücklich F, Suárez S. Tribological behavior of self-lubricating carbon nanoparticle reinforced metal matrix composites. Wear 2018;408–409:72–85. https://doi.org/10.1016/j. wear.2018.05.003.
- [24] Kogut L, Etsion I. Elastic-plastic contact analysis of a sphere and a rigid flat. J Appl Mech 2002;69:657–62. https://doi.org/10.1115/1.1490373.
- [25] Chang WR, Etsion I, Bogy DB. An elastic-plastic model for the contact of rough surfaces. J Tribol 1987;109:257–63. https://doi.org/10.1115/1.3261348.
- [26] Zhao Y, Maietta DM, Chang L. An asperity Microcontact model incorporating the transition from elastic deformation to fully plastic flow. J Tribol 2000;122:86–93. https://doi.org/10.1115/1.555332.
- [27] Shankar S, Mayuram MM. A finite element based study on the elastic-plastic transition behavior in a Hemisphere in contact with a rigid flat. J Tribol 2008;130. https://doi.org/10.1115/1.2958081.
- [28] Jackson RL, Green I. On the modeling of elastic contact between rough surfaces. Tribology Transactions 2011;54:300–14. https://doi.org/10.1080/ 10402004.2010.542277.
- [29] Jackson RL, Green I. A statistical model of elasto-plastic asperity contact between rough surfaces. Tribol Int 2006;39:906–14. https://doi.org/10.1016/j. triboint.2005.09.001.
- [30] Greenwood JA, Williamson JBP. Contact of nominally flat surfaces. Proc R Soc Lond A Math Phys Sci 1966;295:300–19. https://doi.org/10.1098/ rspa.1966.0242.
- [31] Ghaednia H, Wang X, Saha S, Xu Y, Sharma A, Jackson RL. A review of elastic-plastic contact mechanics. Appl Mech Rev 2017;69. https://doi.org/ 10.1115/1.4038187.
- [32] Nayak UP, Guitar MA, Mücklich F. A comparative study on the influence of chromium on the phase fraction and elemental distribution in as-cast high chromium cast irons: Simulation vs. experimentation. Metals 2020;10. https://doi. org/10.3390/met10010030.
- [33] Nayak UP, Guitar MA, Mücklich F. Evaluation of etching process parameter optimization in the objective specific microstructural characterization of as-cast and heat treated HCCI alloy. Pract Metallogr 2020;57:688–713. https://doi.org/ 10.3139/147.110682.
- [34] Guitar MA, Suárez S, Prat O, Duarte Guigou M, Gari V, Pereira G, Mücklich F. High chromium cast irons: destabilized-Subcritical secondary carbide precipitation and its effect on hardness and wear properties. J Mater Eng Perform 2018;27:3877–85. https://doi.org/10.1007/s11665-018-3347-1.
- [35] Laird G, Powell GLF. Solidification and solid-state transformation mechanisms in Si alloyed high-chromium white cast irons. Metall Trans A 1993;24:981–8. https:// doi.org/10.1007/BF02656520.
- [36] Nayak UP, Mücklich F, Guitar MA. Time-dependant microstructural evolution and tribological behaviour of a 26 wt% Cr white cast iron subjected to a destabilization heat treatment. Met Mater Int 2023;29:934–47. https://doi.org/10.1007/s12540-022-01276-8.

- [37] Alderete B, Puyol R, Slawik S, Espin E, Mücklich F, Suarez S. Multipurpose setup used to characterize tribo-electrical properties of electrical contact materials. MethodsX 2021;8:101498. https://doi.org/10.1016/J.MEX.2021.101498.
- [38] Green I, Woodruff GW. Poisson ratio effects and critical values in spherical and cylindrical Hertzian contacts. Int J Appl Mech Eng 2005;10:451–62.
- [39] Nayak UP, Suárez S, Pesnel V, Mücklich F, Guitar MA. Load dependent microstructural evolution in an as-cast 26% Cr high chromium cast iron during unlubricated sliding. Friction 2022;10:1258–75. https://doi.org/10.1007/s40544-021-0553-x.
- [40] Tabor D. The hardness of Metals. Oxford (UK): Claredon Press; 1951.
- [41] Pintaude G. Hardness as an indicator of material strength: a critical review. Crit Rev Solid State Mater Sci 2023;48:623–41. https://doi.org/10.1080/ 10408436.2022.2085659.
- [42] Pompel Kugel. Datenblatt. Data sheet; 2020. https://www.kugelpompel.at/uploa d/2312763_DatenblattAluminiumoxidkugelV1.01.pdf. [Accessed 11 November 2020].
- [43] Auerkari P. Mechanical and physical properties of engineering alumina ceramics. Espoo: Technical Research Centre of Finland; 1996.
- [44] ASM International. ASM Handbook: properties and Aelection: irons, steels, and high performance alloys. ASM International; 1990. https://doi.org/10.31399/asm. hb.v01.9781627081610.
- [45] Calcagnotto M, Ponge D, Demir E, Raabe D. Orientation gradients and geometrically necessary dislocations in ultrafine grained dual-phase steels studied by 2D and 3D EBSD. Mater Sci Eng 2010;527:2738–46. https://doi.org/10.1016/j. msea.2010.01.004.
- [46] Sandikoglu A, Gecu R. Microstructural, mechanical and tribological characterization of aluminum-alloyed ductile cast irons based on aluminum content. J Alloys Compd 2021;879:160428. https://doi.org/10.1016/J. JALLCOM.2021.160428.
- [47] Ohser J, Mücklich F. Statistical analysis of microstructures in materials Science. first ed. Wiley; 2000.
- [48] Vander Voort GF. Metallography: Principles and Practice. 1999.
- [49] Jokari-Sheshdeh M, Ali Y, Gallo SC, Lin W, Gates JD. Comparing the abrasion performance of NiHard-4 and high-Cr-Mo white cast irons: the effects of chemical composition and microstructure. Wear 2022;492–493:204208. https://doi.org/ 10.1016/j.wear.2021.204208.
- [50] Abbaschian R, Abbaschian L, Reed-Hill RE. Physical Metallurgy Principles. Stamford, Connecticut (USA): Cengage Learning; 2008.
- [51] Nayak UP, Schäfer F, Mücklich F, Guitar MA. Wear induced Sub-surface deformation characteristics of a 26 Wt% Cr white cast iron subjected to a destabilization heat treatment. Tribol Lett 2023;71. https://doi.org/10.1007/ s11249-022-01683-3.
- [52] Penagos JJ, Ono F, Albertin E, Sinatora A. Structure refinement effect on two and three-body abrasion resistance of high chromium cast irons. Wear 2015;340–341: 19–24. https://doi.org/10.1016/j.wear.2015.03.020.
- [53] Levitas VI, V Idesman A, Olson GB. Continuum modeling of strain-induced martensitic transformation at shear-band intersections. Acta Mater 1998;47: 219–33. https://doi.org/10.1016/S1359-6454(98)00314-0.

- [54] Mao B, Chu S, Wang S. Effect of grain size on the friction-induced martensitic transformation and tribological properties of 304 austenite stainless steel. Metals 2020;10:1–14. https://doi.org/10.3390/met10091246.
- [55] Talonen J, Hänninen H. Formation of shear bands and strain-induced martensite during plastic deformation of metastable austenitic stainless steels. Acta Mater 2007;55:6108–18. https://doi.org/10.1016/j.actamat.2007.07.015.
- [56] Calculator for Conversion between Vickers Hardness Number and SI Units MPa and GPa, (n.d.). https://www.gordonengland.co.uk/hardness/hvconv.htm (accessed August 19, 2024).
- [57] Varney P, Green I. Rough surface contact of curved conformal surfaces: an application to Rotor–Stator Rub. J Tribol 2016;138. https://doi.org/10.1115/ 1.4032786.
- [58] Jackson RL, Green I. A finite element study of elasto-plastic Hemispherical contact against a rigid flat. J Tribol 2005;127:343–54. https://doi.org/10.1115/ 1.1866166
- [59] Green I. Poisson ratio effects and critical values in spherical and cylindrical hertzian contacts. Int J Appl Mech Eng 2005;10:451–62.
- [60] Alderete B, Nayak UP, Mücklich F, Suarez S. Influence of topography on electrical contact resistance of copper-based materials. Surf Topogr 2023;11:025027. https://doi.org/10.1088/2051-672X/ACDFEA.
- [61] Schindelin J, Arganda-Carreras I, Frise E, Kaynig V, Longair M, Pietzsch T, Preibisch S, Rueden C, Saalfeld S, Schmid B, Tinevez JY, White DJ, Hartenstein V, Eliceiri K, Tomancak P, Cardona A. Fiji: an open-source platform for biologicalimage analysis. Nat Methods 2012;9:676–82. https://doi.org/10.1038/ pmeth 2019.
- [62] Neville A, Reza F, Chiovelli S, Revega T. Characterization and corrosion behavior of high-chromium white cast irons. Metall Mater Trans A Phys Metall Mater Sci 2006;37:2339–47. https://doi.org/10.1007/BF02586208.
- [63] Tabrett CP, Sare IR. Fracture toughness of high-chromium white irons: influence of cast structure. J Mater Sci 2000;35:2069–77. https://doi.org/10.1023/A: 1004755511214.
- [64] Doğan ÖN, Hawk JA, Laird G. Solidification structure and abrasion resistance of high chromium white irons. Metall Mater Trans A Phys Metall Mater Sci 1997;28: 1315–28. https://doi.org/10.1007/s11661-997-0267-3.
- [65] Jain AS, Mustafa MI, Sazili MIIM, Chang H, Zhang MX. Effects of destabilization and tempering on microstructure and mechanical properties of a hypereutectic high-chromium cast iron. J Mater Sci 2022;57:15581–97. https://doi.org/ 10.1007/s10853-022-07583-0.
- [66] Salcedo MC, Coral IB, Ochoa GV. Characterization of surface topography with Abbott Firestone curve. Contemporary Engineering Sciences 2018;11:3397–407. https://doi.org/10.12988/ces.2018.87319.
- [67] Bhushan B. Modern Tribology Handbook. CRC Press; 2000. https://doi.org/ 10.1201/9780849377877.
- [68] Deleanu L, Rîpă M, Tomescu L, Hapenciuc M. Tribological characterisation of surface topography using Abbott-Firestone curve. In: National Tribology Conference: 2003. https://www.researchgate.net/publication/237401824.
- [69] International Organization for Standardization. ISO 21920-2:2021 Geometrical product specifications (GPS)-Surface texture: profile-Part 2: terms, definitions and surface texture parameters. www.iso.org; 2021.